

Dynamic Analysis of Rotor Speed and Electrical Torque of Brushless Doubly Fed Induction Generator (BDFIG) Under Symmetrical and Unsymmetrical Faults

Javad Mahmoudi^{1,*}, Seyed Zeinolabedin Moussavi² and Esmail Mahmoodi³

¹Electrical and Computer Engineering Department, Shahid Rejaee Teacher Training University, Tehran, Iran

²Faculty of Electrical and Computer Engineering, Shahid Rejaee Teacher Training University, Tehran, Iran

³Faculty of Agricultural Engineering, Shahrood University, Semnan, Iran

Abstract: The brushless doubly fed induction generator (BDFIG) has the potential to be employed as a variable speed wind turbine generator. Owing to brushless configuration of this generator, its reliability is higher than DFIG. Most of the grid faults are unsymmetrical. Hence, this paper analyzes dynamic behavior of BDFIG under symmetrical and unsymmetrical faults and presents dynamic models for both fault types. In order to validate the results of analysis, simulations have been carried out using MATLAB/Simulink software. Then, the control winding (CW) current is compared under symmetrical and unsymmetrical faults.

Keywords: Brushless doubly fed induction generator (BDFIG), Grid faults, Rotor speed, Dynamic modeling, Current winding.

1. INTRODUCTION

The evolution of technology related to wind systems industry led to the development of variable speed wind turbines that present advantages compared to the fixed speed wind turbines.

Thereupon, connection of wind farms to grid and analysis and improvement of their dynamic behavior regarding new grid codes have become important issues [1, 2].

The low-voltage ride-through capability of wind turbines with doubly-fed induction generators (DFIGs) has been widely studied in literature e.g. [3-5].

Also, many papers have been presented BDFIG modeling and control. An equivalent circuit is suggested and validated by means of experiments in [6]. A rotor flux oriented control schemes presented in [7, 8] and a unified reference frame d-q model is verified experimentally in [9].

A brief description on structure of BDFIG, fundamentals of operation and its dynamic model for two sequences of machine is presented. In other part of this paper, the variations of fluxes and currents are analyzed using d-q model and the simulation results for speed and currents are presented at the end. The

analysis is based on a simplified vector model developed for the BDFIG with a nested-loop type of rotor in LVRT under three phase voltage dip [10, 11].

2. BDFIG STRUCTURE AND MODELING

The BDFIG comprises two stator windings with different pole numbers to avoid direct coupling. The nested-loop type of rotor is the most well-known [11]. The power winding (PW) is connected to mains and the control winding (CW) is fed by a fractionally rated power electronic converter, as shown in Figure 1. The shaft angular speed, ω_r is determined as:

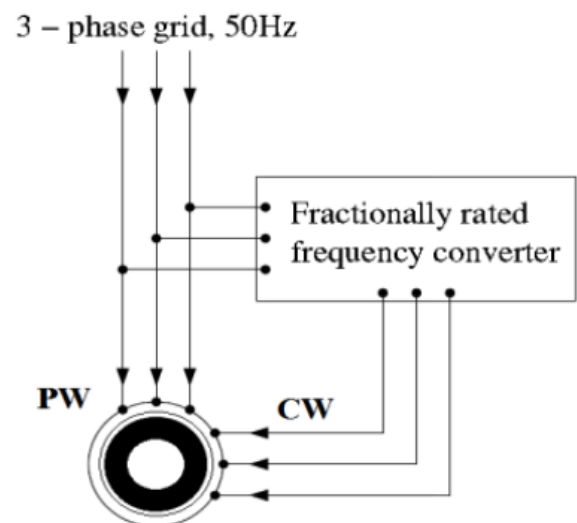


Figure 1: BDFIG structure.

$$\omega_r = \frac{\omega_p + \omega_c}{p_p + p_c} \quad (1)$$

*Address correspondence to this author at the Electrical and Computer Engineering Department, Shahid Rejaee Teacher Training University, Tehran, Iran; Tel: +98-915-372-7855; Fax: +98-585-622-6450; E-mail: jmahmoudi66@gmail.com

Where p_p , p_c , ω_p and ω_c are the PW and CW pole pair numbers and PW and CW angular frequencies, respectively. The BDFIG d-q model in the p_p pole pair synchronously rotating reference frame is stated as [11, 12]:

$$\lambda_p = L_p i_p + L_{pr} i_r \quad (2)$$

$$\lambda_c = L_c i_c + L_{cr} i_r \quad (3)$$

$$\lambda_r = L_r i_r + L_{pr} i_p + L_{cr} i_c; \quad (4)$$

$$v_p = R_p i_p + \frac{d(\lambda_p)}{d(t)} + j\omega_p \lambda_p \quad (5)$$

$$v_c = R_c i_c + \frac{d(\lambda_c)}{d(t)} + j(\omega_p - N_r \omega_r) \lambda_c \quad (6)$$

$$v_r = R_r i_r + \frac{d(\lambda_r)}{d(t)} + j(\omega_p - p_p \omega_r) \lambda_r = 0; \quad (7)$$

$$T_e = -\frac{3}{2} * p_p \text{Im}(\lambda_p^* i_p) - \frac{3}{2} * p_c \text{Im}(\lambda_c i_c^*) \quad (8)$$

$$(T_m - T_e) = J \frac{d(\omega_r)}{d(t)} + B \omega_r \quad (9)$$

PI controllers have been used for speed and PW reactive power control by adjusting v_{qc} and v_{dc} , respectively [13].

Neglecting R_p in (5) leads to (10) and (11) for positive [13] and negative sequence fluxes of PW under fault conditions, respectively. These equations are in the PW reference frame.

$$\lambda_{p+} \approx \frac{V_{p-f}}{\omega_p} e^{j\omega_p t} + \frac{V_{p-0} - V_{p-f}}{\omega_p} e^{-\sigma t} \quad (10)$$

$$\lambda_{p-} \approx \frac{V_{p-f}}{-\omega_p} e^{-j\omega_p t} + \frac{V_{p-0} - V_{p-f}}{-\omega_p} e^{-\sigma t} \quad (11)$$

Combining (2)-(11) and neglecting rotor resistance, positive and negative sequence components of the CW voltage in the CW stationary reference frame are obtained as (12)-(14) with equivalent circuit model as Figure 2.

$$R'_c = R_c + \left(\frac{L_{pr} L_{cr}}{L_p L_r - L_{pr}^2} \right)^2 \quad (12)$$

$$L'_c = L_c - \frac{L_{pr} L_{pr}^2}{L_p L_r - L_{pr}^2}$$

$$v_c^+ = R'_c i_c^+ + L'_c \frac{d(i_c^+)}{d(t)} + E_c^+ \quad (13)$$

$$v_c^- = R'_c i_c^- + L'_c \frac{d(i_c^-)}{d(t)} + E_c^-$$

$$\begin{aligned} E_c^{'+} &= E_{c1}^{'+} + E_{c2}^{'+} \\ &= \frac{1}{\omega_p} \frac{L_{pr} L_{cr}}{L_p L_r - L_{pr}^2} \left\{ \left(\frac{L_r R_p}{L_p L_r - L_{pr}^2} + j(N_r \omega_r - \omega_p) \right) V_{p-f} e^{j(N_r \omega_r - \omega_p)t} \right. \\ &\quad \left. + \left(\frac{L_r R_p}{L_p L_r - L_{pr}^2} + jN_r \omega_r \right) (V_{p-0} - V_{p-f}) e^{j(N_r \omega_r t - \sigma t)} \right\} \quad (14) \end{aligned}$$

$$\begin{aligned} E_c'^- &= E_{c1}'^- + E_{c2}'^- \\ &= \frac{1}{\omega_p} \frac{L_{pr} L_{cr}}{L_p L_r - L_{pr}^2} \left\{ \left(\frac{L_r R_p}{L_p L_r - L_{pr}^2} - j(N_r \omega_r + \omega_p) \right) V_{p-f} e^{j(N_r \omega_r + \omega_p)t} \right. \\ &\quad \left. + \left(\frac{L_r R_p}{L_p L_r - L_{pr}^2} - jN_r \omega_r \right) (V_{p-0}^- - V_{p-f}^-) e^{j(N_r \omega_r t - \sigma t)} \right\} \quad (15) \end{aligned}$$

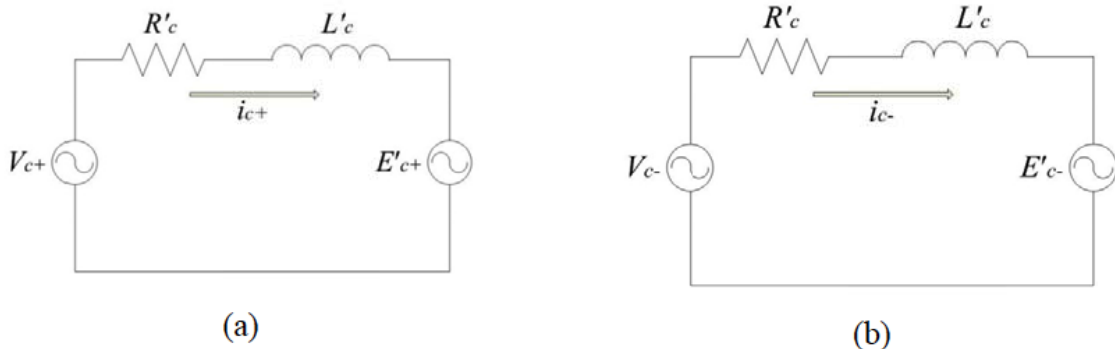


Figure 2: The transient CW model for (a) positive sequence and (b) negative sequence.

In (12), R'_c and L'_c are transient resistance and inductance of CW under – symmetrical or unsymmetrical voltage dip conditions, respectively.

As mentioned in [13], $E'_c{}^+$ is a positive sequence that rotates in the same direction as the injected voltage and $E'_c{}^-$ is a negative sequence EMF that rotates in the opposite direction as the injected voltage, i.e. the EMF frequency of CW is $-\omega_p$ with respect to rotor.

The equations (14) and (15) are EMF of CW during voltage dip. As can be seen from (14) and (15), the EMF has two parts. The first part, $E'_{c1}{}^\pm$, depends upon pre-fault terminal voltage (V_{0-p}) of BDFIG and the second one, $E'_{c2}{}^\pm$, depends on severity of voltage dip ($V_{p-f} - V_{p-0}$). On the other hand, the fault type affects on the induced EMF by changing the frequency. It means that in negative sequence, the value of ($N_r\omega_r + \omega_p$) is larger than in positive sequence ($N_r\omega_r - \omega_p$).

Consequently, the EMF of CW depends on the pre-fault terminal voltage and rotor speed.

Hence, the CW current can be calculated by (16) and (17).

$$i_c^+ = I_{c1}^+ e^{-\frac{R'_c t}{L'_c}} + I_{c2}^+ e^{j(N_r\omega_r - \omega_p)t} + I_{c3}^+ e^{jN_r\omega_r t_c - \sigma t} \quad (16)$$

$$i_c^- = I_{c1}^- e^{-\frac{R'_c t}{L'_c}} + I_{c2}^- e^{j(N_r\omega_r + \omega_p)t} + I_{c3}^- e^{jN_r\omega_r t_c - \sigma t} \quad (17)$$

This currents have two oscillating parts and one DC part (first part). The first part damps rapidly by $\frac{R'_c}{L'_c}$, time constant. This part can be neglected for analysis of fault comparison because of it is same for each faults and negative/positive sequence.

The maximum magnitudes of second and third parts (I_{c2}^\pm, I_{c3}^\pm) are calculated by maximum EMF (for each part separately) and their impedances as (18) and (19).

$$\begin{aligned} \max(i_c^+) &= \max(I_{c2}^+ e^{j(N_r\omega_r - \omega_p)t} + I_{c3}^+ e^{jN_r\omega_r t_c - \sigma t}) \\ &= \frac{\max(E'_{c1}^+)}{Z_c^+} + \frac{\max(E'_{c2}^+)}{\sqrt{(R'_c)^2 + L_c^2 (N_r\omega_r)^2}} \end{aligned} \quad (18)$$

$$\begin{aligned} \max(i_c^-) &= \max(I_{c2}^- e^{j(N_r\omega_r + \omega_p)t} + I_{c3}^- e^{jN_r\omega_r t_c - \sigma t}) \\ &= \frac{\max(E'_{c1}^-)}{Z_c^-} + \frac{\max(E'_{c2}^-)}{\sqrt{(R'_c)^2 + L_c^2 (N_r\omega_r)^2}} \end{aligned} \quad (19)$$

Regarding (14) and (15), the maximum magnitude of EMF ($E'_{c1}{}^\pm, E'_{c2}{}^\pm$) is obtained as:

$$\begin{aligned} \max(E'_{c1}{}^\pm) &= \frac{1}{\omega_p} \frac{L_{pr} L_{cr}}{L_p L_r - L_{pr}^2} \\ &\left(\sqrt{\left(\frac{R_p L_r}{L_p L_r - L_{pr}^2} \right)^2 + (N_r \omega_r \pm \omega_p)^2} \right) V_{p-0}^\pm \end{aligned} \quad (20)$$

$$\begin{aligned} \max(E'_{c2}{}^\pm) &= \frac{1}{\omega_p} \frac{L_{pr} L_{cr}}{L_p L_r - L_{pr}^2} \\ &\left(\sqrt{\left(\frac{R_p L_r}{L_p L_r - L_{pr}^2} \right)^2 + (N_r \omega_r)^2} \right) (V_{p-0}^\pm - V_{p-f}^\pm) \end{aligned} \quad (21)$$

Similarly, the maximum EMF is calculated for post-fault conditions as follows:

$$\begin{aligned} \max(E'_{c1}{}^\pm) &= \frac{1}{\omega_p} \frac{L_{pr} L_{cr}}{L_p L_r - L_{pr}^2} \\ &\left(\sqrt{\left(\frac{R_p L_r}{L_p L_r - L_{pr}^2} \right)^2 + (N_r \omega_r \pm \omega_p)^2} \right) V_{p-f}^\pm \end{aligned} \quad (22)$$

$$\begin{aligned} \max(E'_{c2}{}^\pm) &= \frac{1}{\omega_p} \frac{L_{pr} L_{cr}}{L_p L_r - L_{pr}^2} \\ &\left(\sqrt{\left(\frac{R_p L_r}{L_p L_r - L_{pr}^2} \right)^2 + (N_r \omega_r)^2} \right) (V_{p-f}^\pm - V_{p-0}^\pm) \end{aligned} \quad (23)$$

The term $\left(\frac{1}{\omega_p} \frac{L_{pr} L_{cr}}{L_p L_r - L_{pr}^2} \right)$ is the same for pre- and post-fault conditions as well as symmetrical and unsymmetrical faults. This term is shown by L in the following.

In (22) and (23), the term $\left(\frac{R_p L_r}{L_p L_r - L_{pr}^2} \right)$ is negligible in comparison to $(N_r\omega_r \pm \omega_p)^2$ and $(N_r\omega_r)^2$ under faults. The positive and negative sequences of EMF can be presented as Tables 1 and 2 for fault-on and post-fault conditions, respectively.

Table 3 shows the transient impedance in both of sequences. As can be seen, the transient impedance is higher in the case of negative sequence.

Table 1: Maximum EMF of CW for both Sequences During Voltage Dip Recovery

Sequence	EMF _{max}	
	E'_{c1-max}	E'_{c2-max}
Positive sequence	$L(N_r\omega_r - \omega_p)V_{p-f}^+$	$L(N_r\omega_r)(V_{p-0} - V_{p-f}^+)$
Negative sequence	$L(N_r\omega_r + \omega_p)V_{p-f}^-$	$L(N_r\omega_r)(V_{p-0} - V_{p-f}^-)$

Table 2: Maximum EMF Induced in the CW after Voltage Recovery

Sequence	EMF _{max}	
	E'_{c1-max}	E'_{c2-max}
Positive sequence	$L(N_r\omega_r - \omega_p)V_{p-0}$	$L(N_r\omega_r)(V_{p-f}^+ - V_{p-0})$
Negative sequence	$L(N_r\omega_r + \omega_p)V_{p-0}$	$L(N_r\omega_r)(V_{p-f}^- - V_{p-0})$

Table 3: Maximum EMF of CW for both Sequences During Voltage Dip Recovery

Sequence	Transient impedance of CW $Z'_c = R'_c + jX'_c$	
	R'	X'_c
Positive sequence	$R_c + \left(\frac{L_{pr}L_{cr}}{L_pL_r - L_{pr}^2}\right)^2$	$\left(L_c - \frac{L_{pr}L_{cr}^2}{L_pL_r - L_{pr}^2}\right)(N_r\omega_r - \omega_p)$
Negative sequence	$R_c + \left(\frac{L_{pr}L_{cr}}{L_pL_r - L_{pr}^2}\right)^2$	$\left(L_c - \frac{L_{pr}L_{cr}^2}{L_pL_r - L_{pr}^2}\right)(N_r\omega_r + \omega_p)$

As it can be seen from Table 1, the first part of EMF (E'_{c1-max}) depends on $N_r\omega_r \pm \omega_p$ whereas the second part is the same for both sequences. This means that the first part of EMF will be greater for unsymmetrical faults with equal voltage dip severity due to their negative sequence. On the other hand, the second part is independent from sequences and terminal voltage (V_{p-f}^\pm) determines its maximum magnitude. Table 4 shows this EMF for 3-phase, 2-phase and 1-phase to ground faults in the PW terminals. The terminal voltages are stated as:

$$\begin{aligned} V_a &= V_m \cos(\omega_p t); V_b = V_m \cos(\omega_p t - 120); \\ V_c &= V_m \cos(\omega_p t + 120) \end{aligned} \tag{24}$$

As shown in Figure 3, voltage dips of 0.75% for 100 ms at 240 V are considered in accordance to E. ON Netz grid code for symmetrical and unsymmetrical faults.

The zero sequence voltage is smaller than the others, so it can be negligible for calculation of EMF maximum magnitude. On the other hand, cross coupling don't make between PW and CW because of its zero frequency ($\omega_p = 0$) then DC fluxes which produced by zero sequence can't induce CW voltage and current. Therefore:

$$V_{p-f}^\pm = \sqrt{V_{d-f}^2 + V_{q-f}^2 + V_{0-f}^2} \approx \sqrt{V_{d-f}^2 + V_{q-f}^2} \tag{25}$$

V_{p-f} has close values for 3-phase and 2-phase fault ($V_{p-f} \approx 0.3V_m$). Hence E'_{c1-max} of negative sequence is higher than that of positive sequence. Also, E'_{c2-max} is the same for both of sequences? Hence, the EMF of 2-phase faults is higher than that of 3-phase faults. Under 1-phase fault conditions, V_{p-f} is higher than other fault types and hence, the second part of EMF will be very low.

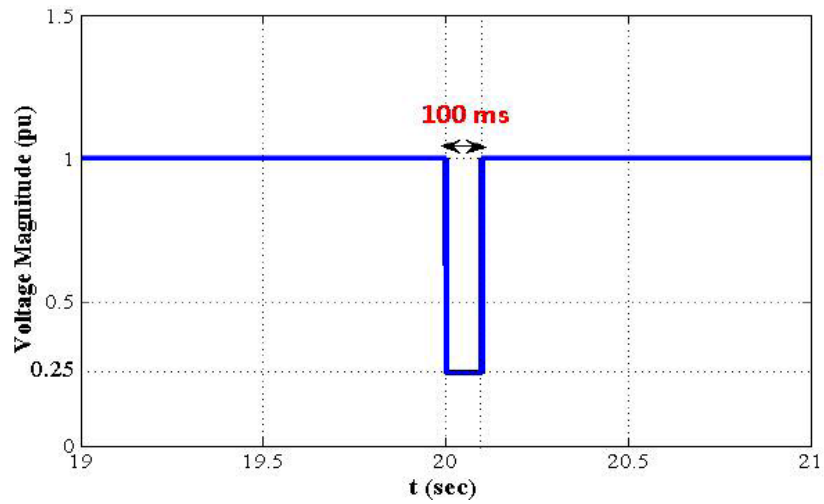


Figure 3: E. ON Netz grid code for all the fault types.

Table 4: PW Terminal Voltage (V_{p-f}) During Different Voltage Dip Types

Fault type	d-q-0 Voltage
3-phase	$v_{q-f} = \frac{2}{3} \begin{bmatrix} \cos(\omega_p t) & \cos(\omega_p t - 120) & \cos(\omega_p t + 120) \end{bmatrix} \begin{bmatrix} 0.25V_m \cos(\omega_p t) \\ 0.25V_m \cos(\omega_p t - 120) \\ 0.25V_m \cos(\omega_p t + 120) \end{bmatrix} = 0.25V_m$ $v_{d-f} = \frac{2}{3} \begin{bmatrix} \sin(\omega_p t) & \sin(\omega_p t - 120) & \sin(\omega_p t + 120) \end{bmatrix} \begin{bmatrix} 0.25V_m \cos(\omega_p t) \\ 0.25V_m \cos(\omega_p t - 120) \\ 0.25V_m \cos(\omega_p t + 120) \end{bmatrix} = 0$ $v_{0-f} = 0$
2-phase	$v_{q-f} = \frac{2}{3} \begin{bmatrix} \cos(\omega_p t) & \cos(\omega_p t - 120) & \cos(\omega_p t + 120) \end{bmatrix} \begin{bmatrix} 0.25V_m \cos(\omega_p t) \\ 0.25V_m \cos(\omega_p t - 120) \\ V_m \cos(\omega_p t + 120) \end{bmatrix} = V_m (-0.25 \sin(2\omega_p t))$ $v_{d-f} = \frac{2}{3} \begin{bmatrix} \sin(\omega_p t) & \sin(\omega_p t - 120) & \sin(\omega_p t + 120) \end{bmatrix} \begin{bmatrix} 0.25V_m \cos(\omega_p t) \\ 0.25V_m \cos(\omega_p t - 120) \\ V_m \cos(\omega_p t + 120) \end{bmatrix} = V_m (-0.25)(\sin(2\omega_p t) + \sin(2\omega_p t + 240))$ $v_{0-f} = \frac{2}{3} \begin{bmatrix} \frac{1}{2} & \frac{1}{2} & \frac{1}{2} \\ \frac{1}{2} & \frac{1}{2} & \frac{1}{2} \\ \frac{1}{2} & \frac{1}{2} & \frac{1}{2} \end{bmatrix} \begin{bmatrix} 0.25V_m \cos(\omega_p t) \\ 0.25V_m \cos(\omega_p t - 120) \\ V_m \cos(\omega_p t + 120) \end{bmatrix} = V_m (0.25)(\cos(\omega_p t - 120))$
1-phase	$v_{q-f} = \frac{2}{3} \begin{bmatrix} \cos(\omega_p t) & \cos(\omega_p t - 120) & \cos(\omega_p t + 120) \end{bmatrix} \begin{bmatrix} 0.25V_m \cos(\omega_p t) \\ V_m \cos(\omega_p t - 120) \\ V_m \cos(\omega_p t + 120) \end{bmatrix} = V_m (0.75 + 0.25 \sin(2\omega_p t))$ $v_{d-f} = \frac{2}{3} \begin{bmatrix} \sin(\omega_p t) & \sin(\omega_p t - 120) & \sin(\omega_p t + 120) \end{bmatrix} \begin{bmatrix} 0.25V_m \cos(\omega_p t) \\ V_m \cos(\omega_p t - 120) \\ V_m \cos(\omega_p t + 120) \end{bmatrix} = (-0.25)V_m \sin(2\omega_p t)$ $v_{0-f} = \frac{2}{3} \begin{bmatrix} \frac{1}{2} & \frac{1}{2} & \frac{1}{2} \\ \frac{1}{2} & \frac{1}{2} & \frac{1}{2} \\ \frac{1}{2} & \frac{1}{2} & \frac{1}{2} \end{bmatrix} \begin{bmatrix} 0.25V_m \cos(\omega_p t) \\ V_m \cos(\omega_p t - 120) \\ V_m \cos(\omega_p t + 120) \end{bmatrix} = V_m (-0.25)(\cos(\omega_p t - 120))$

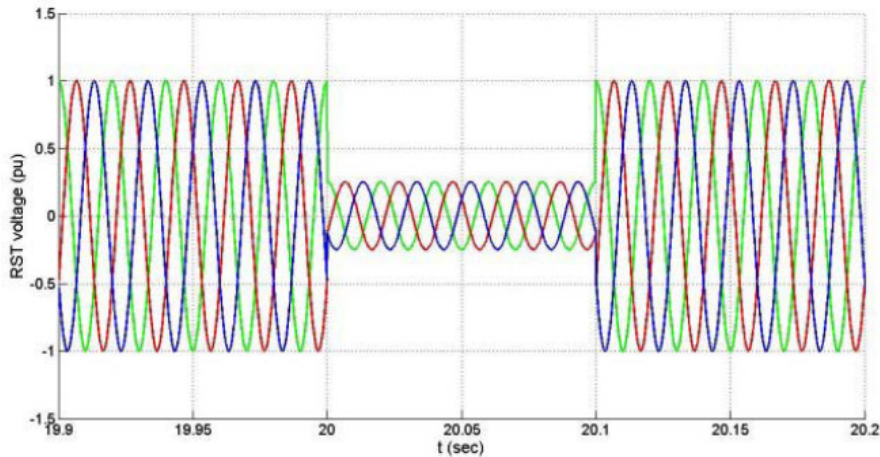


Figure 4: The abc PW voltage.

As mentioned earlier, the EMF of 2-phase fault has the greatest value among the faults. Although this results in increased induced current in the CW, but the transient impedance will also be higher during this type of fault (see Table 3). Obviously, higher transient impedance leads to more highly damped oscillations of electromagnetic torque.

3. SIMULATION AND VALIDATION

The machine model is implemented in MATLAB/Simulink with the parameters given in the Appendix. The nominal torque of 100 Nm and the rated grid voltage of 240 V are applied before voltage dip.

When the E. ON Netz is applied to PW terminals for symmetrical and unsymmetrical faults, following results obtained.

3.1. The 3-Phase Fault

Applying the fault code on PW caused to terminal voltage drop then the fluxes decrease in air gap. The

rotor speed increases by this flux growth reduction, therefore the electromagnetic torque try to control it then T_e decreases.

A three phase voltage dip is applied at $t=20s$ on the generator terminals, as shown in Figure 4. The variation of rotor speed and electromagnetic torque is illustrated in Figures 5 and 6, respectively.

As can be seen from Figure 6, T_e increases when the fault occurs. This is because of instant reduction of flux in CW. The fluctuations after voltage recovery are more than when fault occurs. This is caused by low speed and torque before recovery which results high overshoot when voltage returns to nominal value.

3.2. The 2-Phase Fault

In this part, 2-phase to ground fault analyzes. By grounding of b and c phases of PW, following results obtained. As mentioned before, the fluctuation of T_e is more than symmetrical fault because of the negative sequence of EMF.

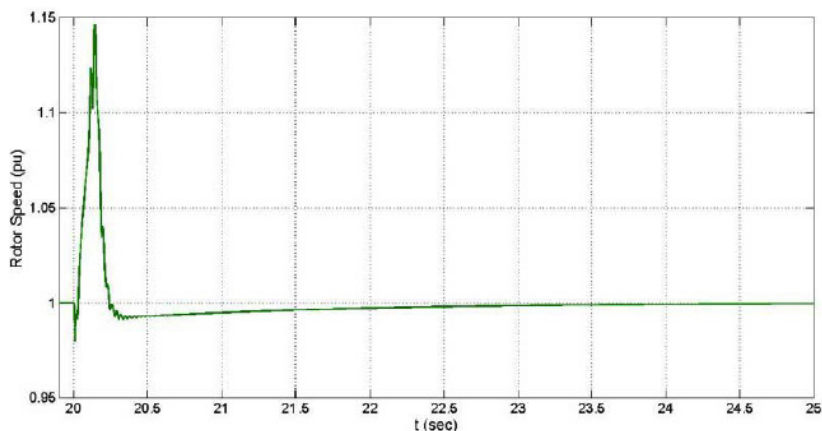


Figure 5: The rotor speed under 3-phase fault.

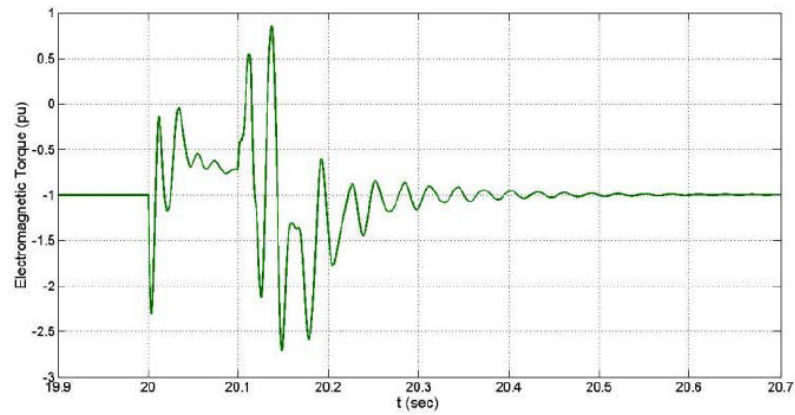


Figure 6: The electromagnetic torque under 3-phase fault.

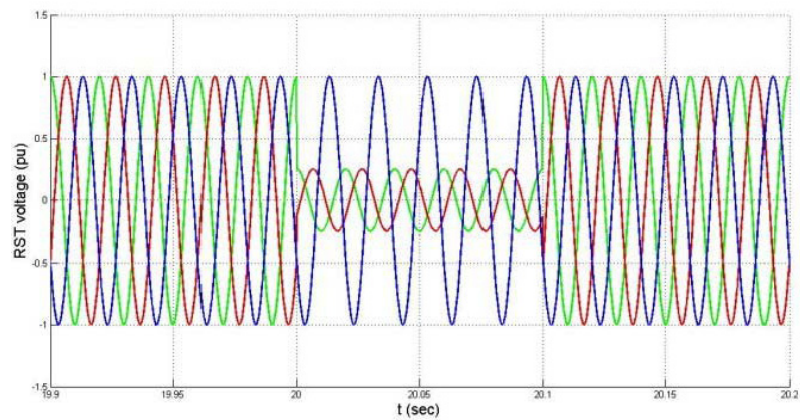


Figure 7: The abc PW voltage.

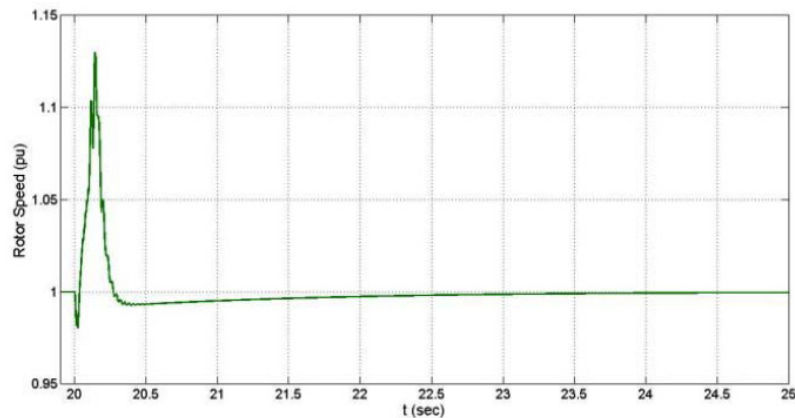


Figure 8: The rotor speed under 2-phase fault.

When a two-phase to ground fault occurs, the value of T_e is lower than 3-phase fault. As it represented, the fluxes in 2-phase fault have lower reduction than 3-phase. Therefore, the speed and T_e were greater.

On the other hand, due to rotated field at reverse direction, the torque will have more fluctuations than the case of three phase faults.

3.3. The 1-Phase Fault

When this fault occurs, the fault-on voltage (V_{p-f}) is higher than other fault types. This results in less reduction of the PW flux linkage and hence, less fluctuation on the electromagnetic torque. Figures 10 to 12 show the terminal voltage, rotor speed and electromagnetic torque for this fault type, respectively.

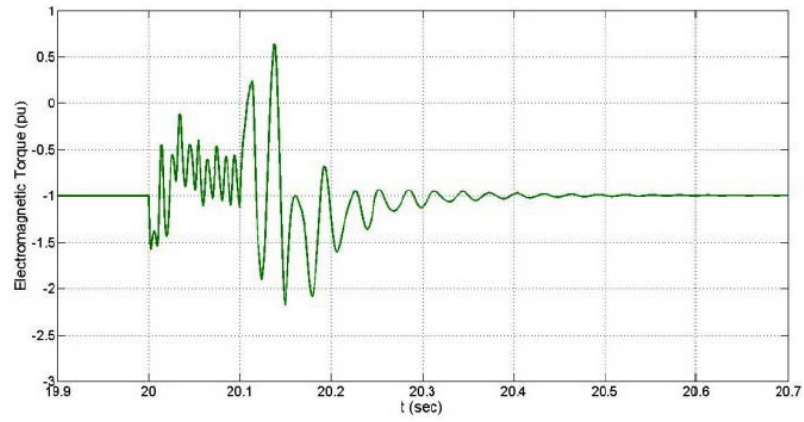


Figure 9: The electromagnetic torque under 2-phase fault.

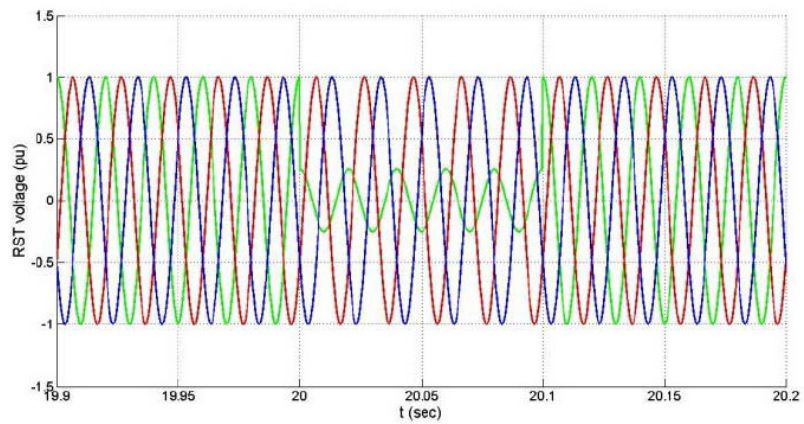


Figure 10: The abc PW voltage.

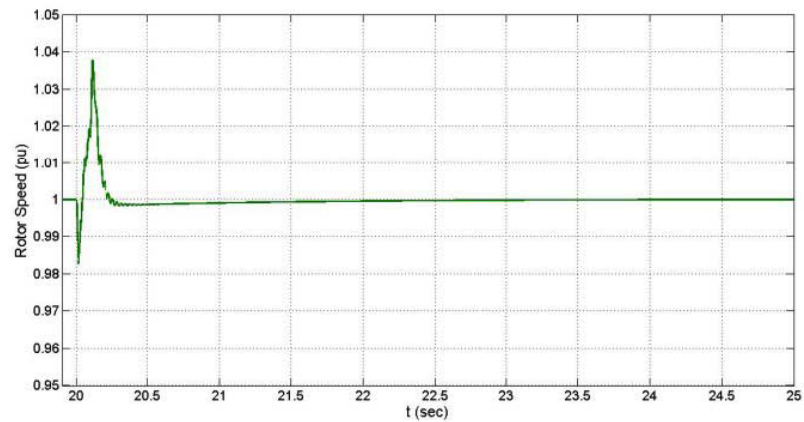


Figure 11: The rotor speed under 1-phase fault.

The rotor speed and electromagnetic torque have lower fluctuations than 3-phase and 2-phase faults as it analyzed before.

However, as observed in the simulation results, damping of fluctuations is higher than other fault types because of two reasons; One, lower dip voltage and second, larger transient impedance.

3.4. CW Current

In order to compare the influence of different types of faults on BDFIG, the CW current peak should be compared.

$$I_{cw} = \sqrt{I_{d-c}^2 + I_{q-c}^2} \tag{26}$$

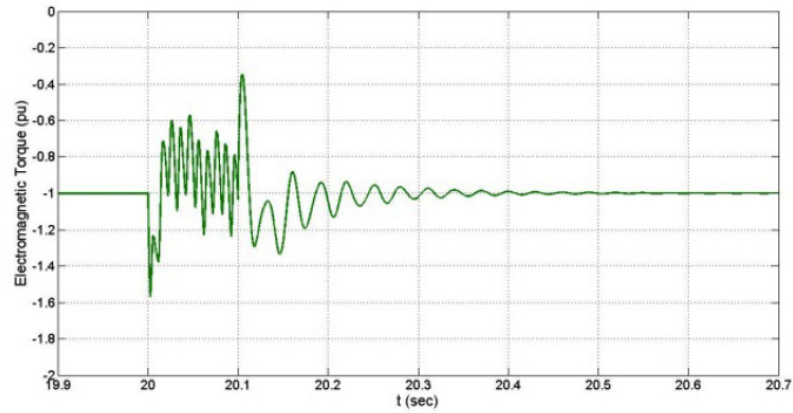


Figure 12: The electromagnetic torque under 1-phase fault.

Another criterion is the settling time of CW current (the time required for reaching CW current to 95% of steady state current) and number of peaks up on 1.5 pu. These factors are shown in Table 5. Figures 13 to 15 show the CW current under different fault conditions.

As shown in Figures 13 to 15, the CW current has higher peak value under 2-phase fault conditions. Fluctuation of post-fault CW current of 2-phase fault is lower than that of 3-phase fault due to higher transient impedance. The EMF amplitude is the smallest in the case of 1-phase to ground fault. Thereupon, the peak

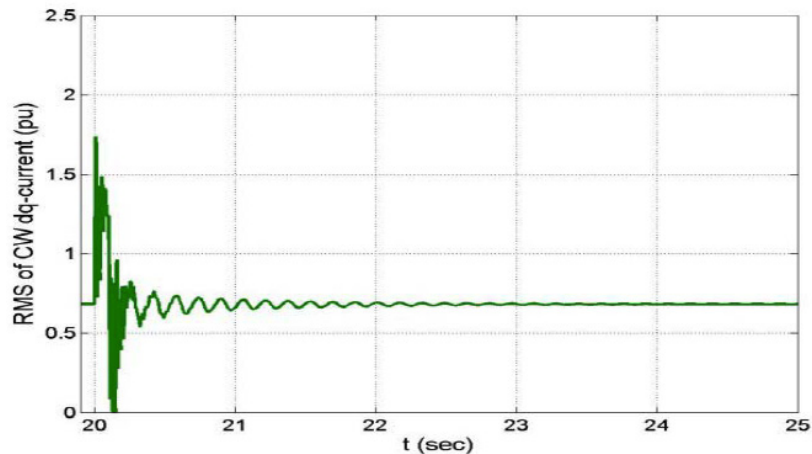


Figure 13: CW current during the 3-phase fault.

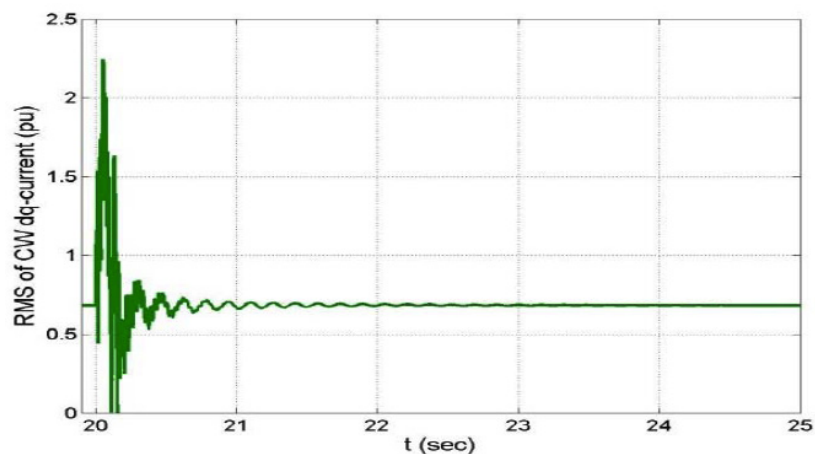


Figure 14: CW current under the 2-phase fault.

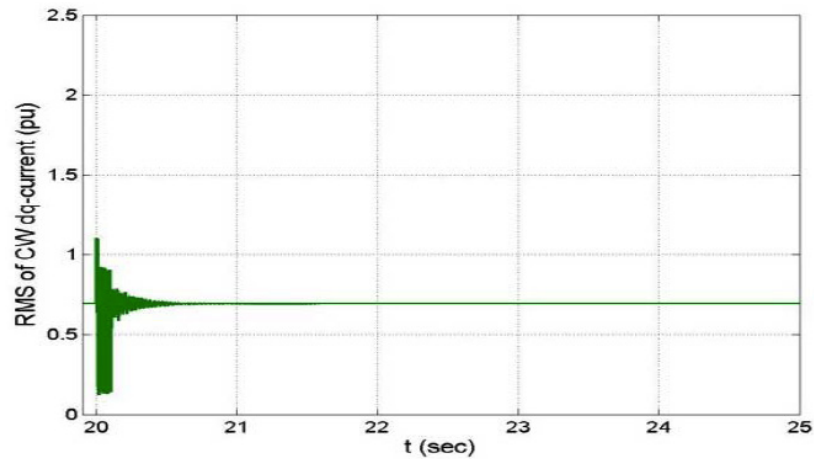


Figure 15: CW current under 1-phase to ground fault.

Table 5: The Criteria for Comparison of I_{cw} for each Fault Type

Fault type	Peak value of I_{cw} (pu)	Settling time (sec)	Number of peaks upon 1.5 pu
3-phase to ground	1.75	2.88	2
2-phase to ground	2.25	2.07	7
1-phase to ground	1.15	0.43	0

value of CW current under this fault is the lowest, too. On the other hand, negative transient impedance leads to highly damped CW current.

The fluctuation of CW current during 2-phase fault is 7 times upon 1.5 pu (see Table 5). This can damage the convertor switches.

As expected, the simulation results validate dynamic model analysis. It is obtained from theoretical analysis and simulations that 2-phase fault leads to

higher peak value of CW current among various types of faults. However, the CW current damping is the highest in the case of 2-phase fault because of higher transient impedance.

4. CONCLUSION

Dynamic performance of BDFIG is presented in different types of faults and the simulation results are used to validate the analysis. The mathematical dq model is used to obtain the induced EMF in the CW.

APPENDIX

Table A1: Prototype BDFIG Specifications

Parameter	Value	Parameter	Value
f_p	50 Hz	Frame size	D180
L_p	0.3498 H	p_p	2
L_c	0.3637 H	p_c	4
L_r	0.0044521 mH	N_r	6
L_{pr}	0.0031 H	Stator slots	48
L_{cr}	0.0022 H	Rotor slots	36
R_p	2.3 Ω	PW rated voltage	240 V in 50 Hz
R_c	4 Ω	CW rated voltage	240 V in 50 Hz
R_r	0.00012967 Ω	PW rated current	8 A
J	0.53 Kg.m ²	CW rated current	8 A
B	.s	Rated Torque	50 Nm

Unsymmetrical faults have applied to investigate the performance of BDFIG torque and effect of produced EMF of CW in transient state. Then, the dynamic model of BDFIG is implemented in MATLAB/Simulink to verify the results for three-phase, two-phase and single-phase to ground faults. The results show that two-phase to ground leads to maximum EMF with highest oscillation and peak of CW current and hence, it is the most severe fault type from LVRT point of view. Furthermore, when an unsymmetrical fault occurs, the negative sequence fluxes result in oscillations of electromagnetic torque and rotor speed.

REFERENCES

- [1] Grid Connection Code – extra high voltage – Transpowerstromubertragungsgmbh, April 2007-2009. [Online]. Available from: <http://www.tennetso.de>
- [2] Lima FKA, Luna A, Rodrigues P, Watanabe EH, Blaabjerg F. Rotor voltage dynamics in the doubly fed induction generator during grid faults. *IEEE Trans Power Electron* 2010; 25(1): 118-130. <http://dx.doi.org/10.1109/TPEL.2009.2025651>
- [3] McMahon RA, Roberts PC, Wang X, Tavner PJ. Performance of BDFM as generator and motor. *Electr Power Applicat IEE Proc* 2006; 153(2): 289-299. <http://dx.doi.org/10.1049/ip-epa:20050289>
- [4] Lopez J, Sanchis P, Roboam X, Marroyo L. Dynamic behavior of the doubly fed induction generator during three-phase voltage dips. *IEEE Trans Energy Convers* 2007; 22(3): 707-717. <http://dx.doi.org/10.1109/TEC.2006.878241>
- [5] Lopez J, Gubia E, Sanchis P, Roboam X, Marroyo L. Wind turbines based on doubly fed induction generator under asymmetrical voltage dips. *IEEE Trans Energy Convers* 2008; 23(1): 321-330. <http://dx.doi.org/10.1109/TEC.2007.914317>
- [6] Roberts PC, McMahon RA, Tavner PJ, Maciejowski JM, Flack TJ. Equivalent circuit for the brushless doubly fed machine (BDFM) including parameter estimation and experimental verification. *IEE Proc – Electric Power Applicat* 2005; 152: 933-942. <http://dx.doi.org/10.1049/ip-epa:20045106>
- [7] Zhou D, Spee R, Alexander GC. Experimental evaluation of a rotor flux oriented control algorithm for brushless doubly fed machines. *IEEE Trans Power Electron*. 1997; 12(1): 72-78. <http://dx.doi.org/10.1109/63.554171>
- [8] Poza J, Oyarbide E, Roya D, Rodriguez M. Vector control design and experimental evaluation for the brushless doubly fed machine. *IEE Proc – Electric Power Applicat* 2009; 3(4): 247-256. <http://dx.doi.org/10.1049/iet-epa.2008.0090>
- [9] Tohidi S, Zolghadri M, Oraee H, Oraee A. Dynamic modeling of a wind turbine with brushless doubly fed induction generator. *Power Electron Drive Systems Technology Conf PEDSTC 2012*: 490-494. <http://dx.doi.org/10.1109/PEDSTC.2012.6183379>
- [10] Poza J, Oyarbide E, Sarasola I, Rodriguez M. Unified reference frame dq model of the brushless doubly fed machine. *IET Electric Power Applicat* 2009; 153(5): 4220-4228.
- [11] McMahon RA, Wang X, Abdi E, Roberts PJ, Jagiela M. The BDFM as a generator in wind turbines, *Power Electron Motion Control Conf 12th Int 2006*: 1859-1865. <http://dx.doi.org/10.1109/EPEPEMC.2006.4778676>
- [12] Roberts PC. A study of brushless doubly-fed (induction) machines. Ph.D dissertation, University of Cambridge 2005.
- [13] Tohidi S, Oraee H, Zolghadri M, Shao S, Tavner P. Analysis and Enhancement of Low Voltage Ride-through Capability of Brushless Doubly Fed Induction Generator. *IEEE Trans Ind Electron* 2013; 60(3): 1146-1155. <http://dx.doi.org/10.1109/TIE.2012.2190955>

Received on 11-05-2014

Accepted on 10-06-2014

Published on 29-08-2014

DOI: <http://dx.doi.org/10.6000/1929-6002.2014.03.03.8>

© 2014 Mahmoudi *et al.*; Licensee Lifescience Global.

This is an open access article licensed under the terms of the Creative Commons Attribution Non-Commercial License (<http://creativecommons.org/licenses/by-nc/3.0/>) which permits unrestricted, non-commercial use, distribution and reproduction in any medium, provided the work is properly cited.